American Mineralogist, Volume 96, pages 1291–1299, 2011

An experimental study of OH solubility in rutile at 500–900 °C, 0.5–2 GPa, and a range of oxygen fugacities

Clinton V. Colasanti,[1,*] Elizabeth A. Johnson,[2] and Craig E. Manning[1,†]

[1]Department of Earth and Space Sciences, University of California Los Angeles, Los Angeles, California 90095, U.S.A.
[2]Department of Geology and Environmental Science, James Madison University, Harrisonburg, Virginia 22807, U.S.A.

Abstract

The solubility of OH in pure synthetic rutile was experimentally constrained at 0.5–2.0 GPa and 500–900 °C, in equilibrium with four oxygen fugacity (f_{O_2}) buffering mineral assemblages: hematite-magnetite (HM), nickel-nickel oxide (NNO), cobalt-cobalt oxide (CCO), and iron-wüstite (IW). The hydroxyl concentration ([OH], in parts per million H_2O by weight) of equilibrated rutile crystals was characterized by FTIR spectroscopy. Measurements at 1 GPa at individual f_{O_2} buffers demonstrate that [OH] in rutile depends strongly on temperature: at HM, [OH] increases from 48 to 267 ppm as temperature rises from 500 to 900 °C, whereas at NNO, [OH] increases from 108 to 956 ppm over the same temperature range. The [OH] in rutile also increases strongly with decreasing f_{O_2} at any pressure and temperature, and exhibits a slight, linear, positive dependence on pressure at a given temperature and f_{O_2}. The observed systematic dependences on pressure, temperature, and f_{O_2} indicate that hydrogen substitutes into rutile as hydroxyl, (OH), via forward progress of the reaction $Ti^{4+}O_2 + {}^1/_2H_2O = Ti^{3+}O(OH) + {}^1/_4O_2$. Our measured [OH] values are significantly greater than those determined in previous studies on finer-grained, polycrystalline rutile, which likely suffered diffusive loss of H during quenching. This is supported by our observation of narrow, OH-depleted rims on otherwise high-OH run products, pointing to minor but important diffusive H loss from crystal rims during quenching. Fitting of isothermal variations in composition with f_{O_2} at 1 GPa and temperature indicates nearly ideal, multi-site mixing of the TiO_2-TiOOH solid solution. A fit to the entire data set suggests standard volume, enthalpy, and entropy of the hydration reaction of, respectively, 1.90 ± 0.48 cm^3/mol, 219.3 ± 1.3 kJ/mol, and 19.9 ± 1.4 J/(mol·K) (1σ uncertainty). These constraints form the basis for use of [OH] in rutile as a thermobarometer and oxybarometer in experimental and natural systems. The moderate to high [OH] in nominally anhydrous rutile at all investigated temperatures, pressures, and f_{O_2} values imply that Ti^{3+} may be higher than previously suspected in some terrestrial geologic settings.

Keywords: Rutile, experimental petrology, infrared spectroscopy, oxygen fugacity, hydroxyl, nominally anhydrous minerals

Introduction

Rutile is a common accessory mineral in many metamorphic and igneous systems, including eclogites and MARID mantle xenoliths (Vlassopoulos et al. 1993), mélanges associated with subduction zones (Sorensen and Grossman 1993), pegmatites and Barrovian metamorphic environments (Hammer and Beran 1991), and plutonic rocks (Frindt et al. 2004). The presence of rutile in such diverse environments makes it useful in thermobarometry (e.g., Bohlen et al. 1983; Manning and Bohlen 1991; Zack et al. 2002, 2004a; Watson and Harrison 2005; Watson et al. 2006; Zack and Luvizottow 2006; Tomkins et al. 2007; Tropper and Manning 2008; Kapp et al. 2009). In addition, uranium concentrations in natural rutile may be high enough for U-Pb geochronometry (Corfu and Andrews 1986; Mezger et al. 1989, 1991). Rutile also accommodates high field strength elements (HFSE), so it is an excellent monitor of mantle metasomatism, melt source, and mantle composition (e.g., Ryerson and Watson 1987; Ayers and Watson 1991, 1993; Brenan et al. 1994; Stalder et al. 1998; Foley et al. 2000; Rudnick et al. 2000; Klemme et al. 2005). Moreover, rutile's resistance to mechanical and chemical weathering means it can be used to gain insights into sedimentary provenance (Force 1980; Zack et al. 2002, 2004b; Triebold et al. 2007). Rutile is also important for its catalytic and optical properties (e.g., Diebold 2003; Thompson and Yates 2006).

An important geochemical feature of rutile is that natural samples almost always contain significant amounts of water (Johnson 2006; Vlassopoulos et al. 1993). The highest concentrations of up to 3000 ppm H_2O are found in high-pressure metamorphic rocks and mantle samples (e.g., Zhang et al. 2001, 2004; Katayama et al. 2006; Chen et al. 2007; Zhao et al. 2007; Zheng 2009).

The atomic structure of rutile consists of chains of Ti^{4+} octahedra aligned parallel to the crystallographic *c*-axis. The simple structure results in a high (tetragonal) symmetry. Studies using polarized infrared spectroscopy show that structurally bound

* Present Address: Department of Earth and Environmental Sciences, Geophysics, Munich University, Theresienstrasse 41, 80333 Munich, Germany.
† E-mail: manning@ess.ucla.edu

hydrogen in rutile occurs as OH, and that the orientation of the OH vector is perpendicular to the *c*-axis (Rossman and Smyth 1990; Vlassopoulos et al. 1993; Swope et al. 1995). Hydrogen in rutile correlates with the concentration of trivalent cations in excess of pentavalent cations and vacancies (Hammer and Beran 1991; Swope et al. 1995; Bromiley et al. 2004), suggesting H incorporation as isolated protons via a $H^+ + R^{3+} = Ti^{4+}$ type reaction (e.g., Keppler and Bolfan Casanova 2006). In pure, vacancy-free rutile, H incorporation is coupled with Ti reduction via forward progress of the reaction:

$$Ti^{4+}O_2 + {}^1/_2H_2O = Ti^{3+}O(OH) + {}^1/_4O_2 \quad (1)$$

for which the equilibrium constant (K) is

$$K = \frac{a_{Ti^{3+}O(OH)} \cdot f_{O_2}^{1/4}}{a_{Ti^{4+}O_2} f_{H_2O}^{1/2}} \quad (2)$$

where f and a refer, respectively, to fugacity and activity. Equation 2 shows that incorporation of OH in pure rutile via reaction 1 depends on the fugacities of oxygen and H_2O.

We investigated experimentally the relationship between OH solubility in rutile and T, P, f_{O_2}, and f_{H_2O}, over a range of P and T corresponding to crustal high-grade metamorphism and upper-mantle processes. By focusing on pure rutile, we assess the applicability of reaction 1 and establish a baseline for other studies investigating the links between OH and other elemental impurities in rutile. The wide range of experimental conditions also allows robust thermodynamic modeling. This forms the basis for utilization of OH in rutile as a monomineralic thermobarometer and oxybarometer for petrologic studies where it is impractical to use multiphase mineral assemblages to calculate f_{O_2} in natural samples (Frost 1991; Spencer and Lindsley 1981) or to assume a relationship between Fe^{3+}/Fe^{2+} in a melt or mineral and f_{O_2} (McCanta et al. 2004). We use the term "OH solubility" to describe the maximum capacity for OH in rutile at given experimental conditions, and [OH] to refer to analytically determined OH concentrations, in parts per million H_2O by weight.

METHODS

Piston-cylinder experiments

The starting material in this study was taken from a pure, synthetic, rutile boule (Morion Co., Brighton, Massachusetts). The rutile was cut into rectangular pieces that were at least 0.75 mm by 0.5 mm and 2 mm long in the crystallographic *c*-axis direction to minimize loss from diffusion, since hydrogen loss is much faster $\|c$ than $\|a$ (Johnson et al. 1975). For each experiment, a single crystal was loaded into a 2 mm outer diameter (O.D.) inner capsule composed of either Pt or a $Ag_{80}Pd_{20}$ alloy. The choice of inner capsule material depended on the experimental temperature. Platinum inner capsules were used for experiments at $T \geq 600$ °C, but $Ag_{80}Pd_{20}$ was used for inner capsules in experiments at $T < 600$ °C due to its higher H permeability (e.g., Chou 1986). After loading the crystal, the inner capsule was filled with 4–5 mg ultrapure H_2O, tightly crimped, and sealed by arc welding. The capsule was then reweighed to check for water loss during welding; capsules that lost more than 0.01 mg H_2O were discarded. The inner capsule was placed in a 5 mm O.D. Au outer capsule with ~25 µL of ultrapure H_2O and one of the following mineral assemblages for f_{O_2} buffering: hematite-magnetite (HM), nickel-nickel oxide (NNO), or cobalt-cobalt oxide (CCO). A single experiment was performed by adding iron and FeO to H_2O, to produce the buffer assemblage iron-wüstite (IW; see below). Gold was used for outer capsules because it has relatively low hydrogen permeability at the temperatures of this study (e.g., Chou 1986). After loading, the outer capsule was crimped, welded, heated in a 115 °C oven for ≥0.5 h, and then reweighed to check the quality of the weld; if any water was lost, the inner capsule was removed, and the loading process repeated.

The assembled capsule was set horizontally in a 2.54 cm NaCl-graphite furnace assembly to minimize temperature gradients (Manning and Boettcher 1994; Newton and Manning 2000). All experiments employed the piston-out method. Reported pressures are accurate to ±300 bar (0.03 GPa). Temperatures were monitored with $Pt\text{-}Pt_{10}Rh_{90}$ thermocouples (accurate to ±3 °C; uncorrected for the effect of P on emf), which were inserted into the furnace assembly in close proximity to the outer capsule.

Experiments were quenched by cutting power to the graphite furnace, causing T to drop to <100 °C in ~25 s. For each experiment, the capsule was removed from the furnace and soaked in water to remove adhering salt. The capsule was then cut open, and the f_{O_2} buffer removed, opened, and checked for the presence of relevant minerals by optical microscopy and, where necessary, by X-ray powder diffraction. An experiment was considered unsuccessful if the outer capsule did not contain water and all of the required solid buffer phases. Values of f_{O_2} at the HM and CCO buffers were calculated from Chou (1978). In the case of HM, Chou's stated minimum T is 600 °C; however, comparisons with other data sources indicated negligible differences at 500–600 °C. Recent experimental work on CCO at 0.04 GPa (Lemke et al. 2008) supports use of the Chou (1978) equation for this buffer. Values of f_{O_2} at the NNO buffer were from Huebner and Sato (1970). The buffer assemblage for run R51 (Table 1) was Fe metal + synthetic FeO, which at 500 °C is metastable with respect to iron-magnetite (Frost 1991); however, only Fe° and FeO were present after the experiment, so f_{O_2} was taken to be that of the iron-wüstite buffer of Frost (1991). Any discrepancies arising from metastability or nonstoichiometry are negligible, as $\log f_{O_2}$ of IW and IM differ by only ~0.1 at 500 °C and 1 GPa.

Quenched experiments, in which the inner capsule did not contain water, were also considered failures due to H_2O loss during the experiment. Some rutile crystals were crushed during experiments; extracted crystals were used for analysis only if they were at least 1 mm long in the *c*-axis direction.

TABLE 1. Experimental results

Experiment*	f_{O_2} buffer†	P (GPa)	T (°C)	Experiment duration (h)	[OH] in rutile (ppm H_2O)‡
R28	HM	0.5	800	24	130
R50	HM	1	500	24	48
R13	HM	1	600	45	84
R19	HM	1	700	24	102
R2	HM	1	800	39	159
R3 (a_{H_2O}=0.61)	HM	1	800	45.5	171
R14	HM	1	900	20	267
R36	HM	2	800	23	280
R32	HM	2	800	15	227
R20	NNO	0.5	800	10	471
R47	NNO	1	500	20	108
R52	NNO	1	500	2	87
R12	NNO	1	600	42.5	158
R23	NNO	1	650	24	195
R10	NNO	1	700	17	259
R37	NNO	1	725	22.5	343
R18	NNO	1	750	21	498
R5	NNO	1	800	13.5	599
R22	NNO	1	800	2	616
R7 (a_{H_2O}=0.61)	NNO	1	800	12	567
R54	NNO	1	850	4	646
R38	NNO	1	900	9	956
R39	NNO	2	800	32	720
R56	CCO	1	500	17	120
R59	CCO	1	550	18	222
R55	CCO	1	600	29	286
R53	CCO	1	650	4.25	399
R58	CCO	1	700	30.5	623
R51	IW	1	500	91	636

* Pure H_2O used in all experiments except R3 and R7, in which H_2O-CO_2 fluid generated from oxalic acid yielding calculated H_2O activity of 0.61.
† Abbreviations for f_{O_2} buffers: HM, hematite-magnetite; NNO, nickel-nickel oxide; CCO, cobalt-cobalt oxide; IW, iron-wüstite.
‡ [OH] determined using the calibration of Maldener et al. (2001). Errors are 5% relative (1σ).

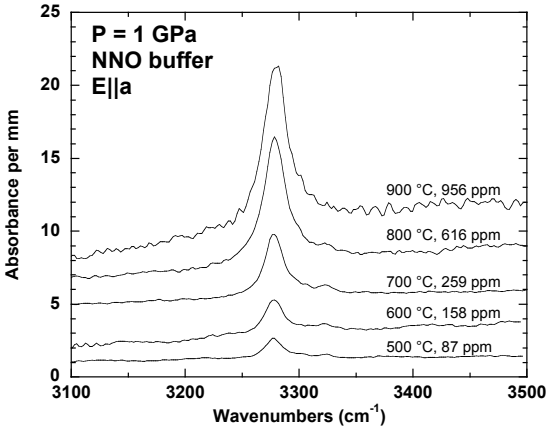

FIGURE 1. Polarized infrared spectra (E||*a*) of structural OH in rutile at 1 GPa, 500–900 °C, and f_{O_2} constrained by the NNO buffer.

Infrared spectroscopy

Doubly polished thin sections (~0.020–0.250 mm thickness) of rutile run products were prepared with the *c* and *a* axes in the plane of the thin section. Polarized mid-infrared (4000–2600 cm^{-1}) spectra were obtained with either the Thermo-Nicolet Magna 860 FTIR spectrometer in the Division of Geological and Planetary Sciences at the California Institute of Technology, Pasadena, California, or the Varian Digilab Exacalibur FTS3000 FTIR spectrometer in the Department of Mineral Sciences, Smithsonian Institution, Washington, D.C. Spectra were obtained using a microscope accessory with rectangular aperture sizes between 30 × 50 µm and 150 × 150 µm at 4 cm^{-1} resolution. Spectra were averaged over 256–1024 scans using a MCT-A detector, KBr beamsplitter, and wire grid infrared polarizer. Whenever possible, polarized measurements were made with E||*a* and E||*c*. For some samples containing high OH concentrations the absorption due to intervalence charge transfer overwhelmed the OH band when E||*c*. In these cases it was possible to obtain only the E||*a* spectrum.

Absolute hydroxyl concentration (c_{OH}, in moles of H_2O per L of rutile) was obtained from a modified form of the Beer-Lambert law via:

$$c_{OH} = \frac{\Delta}{\varepsilon' \times t} \quad (3)$$

in which Δ is the total integrated area of OH bands in the 3200–3350 cm^{-1} region (Fig. 1, computed after Maldener et al. 2001 from $\Delta = 2\Delta_a + \Delta_c$, where Δ_a and Δ_c are, respectively, the integrated areas of the OH bands in E||*a* and E||*c* spectra), ε' is the integrated molar absorption coefficient in L·mol H_2O^{-1}·cm^{-2}, and t is the thickness (path length) of the rutile crystal in centimeters. Three different values have been determined for ε' in rutile: 30235 L·mol H_2O^{-1}·cm^{-2} (Johnson et al. 1973), 6540 L·mol H_2O^{-1}·cm^{-2} (Hammer and Beran 1991), and 38000 ± 4000 L·mol H_2O^{-1}·cm^{-2} (Maldener et al. 2001). In this study, we use ε' from Maldener et al. (2001) for two reasons: (1) this is a revision of an earlier nuclear reaction analysis done by the same group (Hammer 1988), but Maldener et al. (2001) used polarized infrared measurements of rutile; and (2) the Maldener et al. (2001) value is in fairly close agreement (~25%) with the value obtained by Johnson et al. (1973) using a different method (D-H exchange and mass difference).

Uncertainties in [OH] are about ±5% relative (1σ) based on propagation of the error for ε' and errors on repeated measurements of Δ. The [OH] in the starting rutile material was 10 ppm.

RESULTS

Experimental results are given in Table 1. The solubility of OH in rutile was investigated from 500–900 °C, 0.5–2.0 GPa, and over a range of buffered oxygen fugacities. Most experiments were conducted in pure H_2O; however, two runs (R3 and R7) used H_2O-CO_2 mixtures to produce reduced H_2O activity.

In all runs, the starting pale-yellow rutile changed color to medium- to deep-blue (Fig. 2), as also noted in previous studies (e.g., Huntington and Sullivan 1965; Tropper and Manning 2005). This color change results from intervalance charge transfer associated with the reduction of Ti^{4+} to Ti^{3+}, which produces strong and broad optical absorbance centered in the near-IR region (5000–6000 cm^{-1}) (Khomenko et al. 1998). This absorption band extends into the red region of visible light, producing the blue color. Because H^+ concentration increases with Ti^{3+} (reaction 1), the color of rutile provides a qualitative guide to the extent of H^+ substitution: the deeper blue the color, the higher the [OH] in rutile. The color change also limits the range of conditions accessible to the experiments; for example, at f_{O_2} corresponding to the IW buffer, rutile equilibrated at ≥600 °C is expected to be effectively opaque—even in the mid-IR region—at thicknesses that could be obtained practically using our polishing methods.

Run durations needed for equilibration were tested by comparing two 2 h experiments (R22 at 800 °C and R52 at 500 °C, Table 1) with results obtained at the same conditions but longer

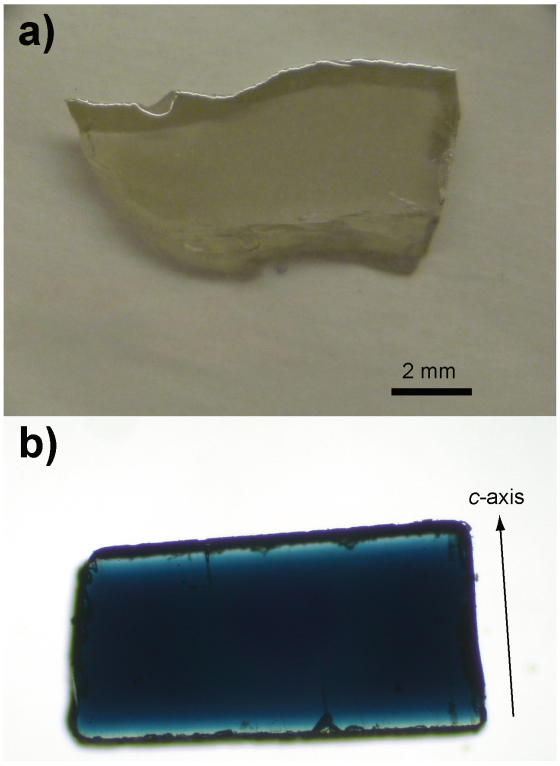

FIGURE 2. (**a**) Reflected-light image of a chip of polished, pale-yellow synthetic rutile, mounted in epoxy. Rough material was cut into oriented rectangles for use as starting crystals. (**b**) Unpolarized transmitted-light images of doubly polished section of product rutile from a preliminary experiment at 800 °C and 1 GPa that was unbuffered with respect to f_{O_2}. Crystal is ~750 µm in the *c*-axis direction and 0.287 mm thick. The crystal in **b** illustrates the dark-blue coloration associated with Ti^{3+}-Ti^{4+} intervalence charge transfer during equilibration at high *P* and *T*, which correlates with an increase in [OH] (reaction 1). The crystal displays 50–75 µm pale-blue rims normal to **c**, which are interpreted to result from diffusive loss of hydrogen in the **c** direction during quenching. Such rims were either absent or less pronounced in f_{O_2}-buffered experiments. (Color online.)

times. The [OH] values were time-independent within error. We conclude that equilibrium is rapidly attained, consistent with high H^+ diffusivity in rutile. Nevertheless, run durations were generally >12 h, except where experimental T was >800 °C.

The [OH] in rutile in pure-H_2O experiments ranges from 48 to 956 ppm H_2O (Table 1) and varies systematically with T, P, and f_{O_2}. At 1 GPa and a given f_{O_2} buffer, OH solubility in rutile increases exponentially with increasing T in the range 500–900 °C (Fig. 3). As predicted by Eqs. 1 and 2, OH solubility in rutile increases as f_{O_2} declines at all T at constant P. Figure 4 shows that at 500 °C and 1 GPa, where we were able to study the greatest range in f_{O_2}, there is a simple inverse linear relationship between log f_{O_2} and log [OH]. In the range 0.5 to 2.0 GPa, rutile shows a linear increase in [OH] with P at 800 °C at both the NNO and HM f_{O_2} buffers (Fig. 5).

Most of the experiments used initially pure H_2O. The very low solubility of rutile in H_2O at all studied conditions (Tropper and Manning 2005; Audétat and Keppler 2005; Antignano and Manning 2008) means that H_2O remained effectively pure in the experiments. Hydrous oxalic acid ($H_2C_2O_4 \cdot 2H_2O$) was added to the inner capsule instead of pure water for two experiments at 800 °C, 1 GPa, and the HM and NNO buffers (Table 1), producing a fluid with H_2O mole fraction (X_{H_2O}) of ~0.5. Calculated H_2 mole fraction is negligibly low at the experimental conditions. At these conditions, H_2O fugacity is reduced by a factor of 0.61 (Aranovich and Newton 1999). Neither experiment yielded a detectable difference in [OH] relative to the equivalent experiments using pure water. This is not surprising, considering that only large changes in f_{O_2} (measured in log units) will have an effect on the concentration of OH, and water activity was only dropped to ~0.61 in the experiments. These data suggest that OH solubility in rutile is relatively insensitive to fluid H_2O content at X_{H_2O} > ~0.5.

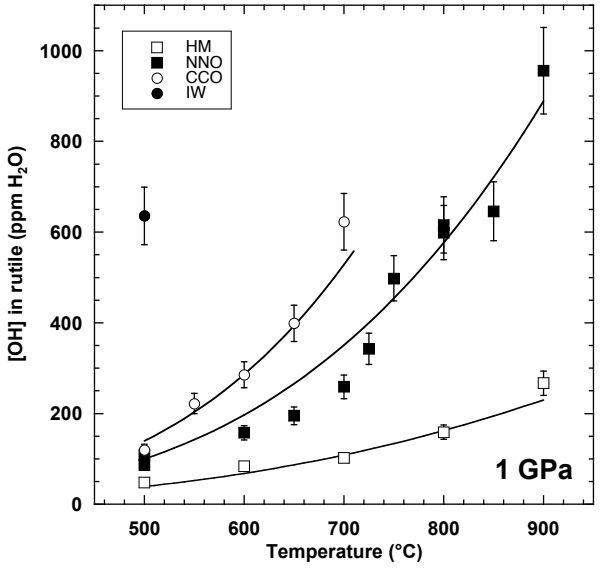

FIGURE 3. Temperature dependence of [OH] in rutile equilibrated with pure H_2O at 1 GPa and four f_{O_2} buffers: iron-wüstite (IW, filled circle), cobalt-cobalt oxide (CCO, open circles), nickel-nickel oxide (NNO, filled squares), and hematite-magnetite (HM, open squares). Error bars are 2σ. Solid curves are from Equation 12 using fit parameters in Table 2.

DISCUSSION

H-substitution mechanism

The experiments demonstrate that there is a systematic dependence of measured [OH] on T, P, and f_{O_2}. This strongly supports the assumption that hydrogen substitution is coupled to Ti^{4+} reduction to Ti^{3+}, and is consistent with the qualitative observation that blue color deepens with increasing [OH]. Alternative substitution mechanisms, via structural defects and damage (e.g., Lu et al. 2001; Bromiley and Shiryaev 2006; Amore Bonapasta et al. 2009; Filippone et al. 2009), would not be expected to show this systematic dependence.

Comparison to previous work

Bromiley and Hilairet (2005) report [OH] in pure rutile at 1100 °C, 2 GPa, and an f_{O_2} approximately equivalent to the NNO buffer. Recalculating their measurements using Maldener et al. (2001) gives [OH] = 72 ± 2 ppm. In contrast, extrapolation of our results at the same f_{O_2} to the same P and T yields [OH] of at least several thousand parts per million (Figs. 3 and 5). Assuming that H_2O saturation was in fact attained in the Bromiley and

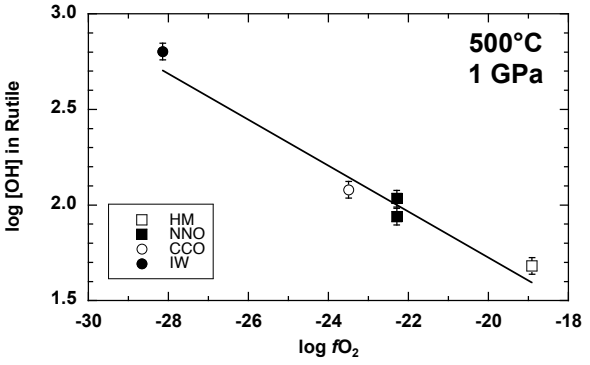

FIGURE 4. Logarithm of [OH] in rutile at 500 °C, 1 GPa, as a function of log f_{O_2}. The two experiments run at the NNO buffer (filled squares) are experiments lasting 2 and 20 h. The absence of a time-dependent difference in [OH] supports the assumption of attainment of equilibrium. Symbols as in Figure 3; error bars are 2σ. Solid curve is from Equation 12 using fit parameters in Table 2.

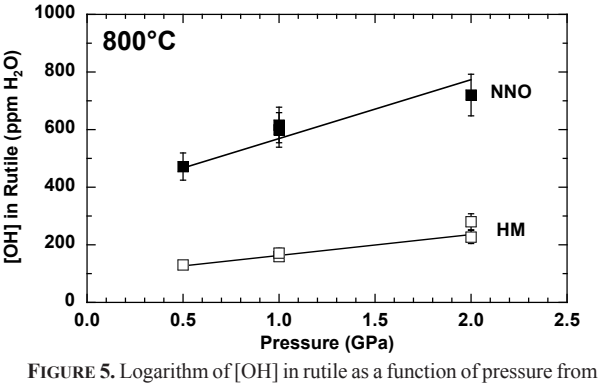

FIGURE 5. Logarithm of [OH] in rutile as a function of pressure from at 800 °C at f_{O_2} buffered by HM and NNO. Symbols as in Figure 3; error bars are 2σ. Solid curves are from Equation 12 using fit parameters in Table 2.

Hilairet (2005) experiments, it is clear that the two studies are highly discrepant.

The most likely explanation for the disparate results is the contrasting effects of quench-related diffusive H loss on rutile of different grain sizes and equilibration *T*. In the Bromiley and Hilairet (2005) study, rutile was ground to a powder and then annealed during experiment to 30–500 μm in diameter. In contrast, our samples were cut at least 1000 μm long in the *c*-axis direction. When combined with the different *T* from which the experiments were quenched, such differences in size could be important if there is significant diffusive proton exchange with H_2O during quenching.

Figure 2 illustrates that rutile rims in our experiments display evidence for diffusive hydrogen loss during quenching. The run product in Figure 2 is from a preliminary unbuffered experiment at 800 °C. The crystal displays a pronounced lighter blue rim at its top and bottom. In contrast, the crystal interior and sides are deeper blue in color. Because measured [OH] is proportional to the depth of the blue color, the observation implies that there was rapid hydrogen loss parallel to the *c*-axis during the ~25 s required to quench this experiment from 800 to <100 °C.

Our inference of rapid diffusive hydrogen loss along the *c*-axis is consistent with studies of H diffusion in rutile (Johnson et al. 1975; Cathcart et al. 1979; Ingrin and Blanchard 2006). Hydrogen diffusion is strongly temperature dependent and significantly faster along the *c*-axis (||*c*) than the *a*-axis (||*a*) due to the alignment of the Ti octahedral chains and the structural channels along rutile's *c*-axis (Johnson et al. 1975). Ignoring likely minor pressure effects, diffusion coefficients (*D*) calculated from Johnson et al. (1975) at 800 °C are $\log D_{||a} = -6.4$ cm^2/s and $\log D_{||c} = -5.5$ cm^2/s. The quench time for our experiments to cool below 100 °C in our experiments was 25 s. The relatively slow thermal diffusivity of rutile will cause the crystal to remain at elevated *T* as the apparatus cools. Assuming a diffusion time (*t*) of 10 s, these *D* values give characteristic diffusion lengths (*h,* where $h = \sqrt{Dt}$) of 55 μm parallel to the *c*-axis and 19 μm parallel to the *a*-axis. The value of $h_{||c}$ agrees closely with the observed width of the low-[OH], pale-blue rims along the *c*-axis (Fig. 2). The value of $h_{||a}$ implies lower but potentially observable H loss along the *a*-axis; however, optical inspection of product crystals revealed no evidence for H loss along *a* in any experiment. It is important to note that the actual change in *T* with time during quenching is nonlinear and its functional form is not known, so these calculations are necessarily approximate.

Applying the same approach to the experiments of Bromiley and Hilairet (2005) at 1100 °C yields $\log D_{||a} = -5.1$ cm^2/s and $\log D_{||c} = -4.9$ cm^2/s, which leads to $h_{||c} = 110$ μm and $h_{||a} = 87$ μm, assuming the same quench times. Because product grain radii in the Bromiley and Hilairet (2005) experiments are 25–250 μm, this calculation reveals that a large fraction of the rutile grains were comparable in size to the characteristic diffusion length scale for H loss, regardless of crystallographic orientation. This assessment used conservative estimates. The experimental apparatus used for our study is optimized for rapid quenching (Manning and Boettcher 1994), and it is unlikely that the quench times of Bromiley and Hilairet (2005) were shorter. Regardless, the higher temperatures of their experiments can be expected to have required longer quenching times. Finally, for this comparison we used an experiment with no f_{O_2} buffer, as in the experiments of Bromiley and Hilairet (2005). We observed qualitatively that pale-blue rims in experiments in which f_{O_2} was controlled by a buffering mineral assemblage were narrower or absent, suggesting that the presence of the buffer improves H retention. Thus, though experimental conditions differed, the much greater [OH] in rutile implied by this study compared to Bromiley and Hilairet (2005) likely arises from diffusive H loss during quench in the latter work. Careful consideration of run-product grain size is essential for accurate assessment of OH solubility, where H diffusivity is high.

TiO_2-TiOOH mixing properties

Constraints on the mixing properties of TiO_2-TiOOH solid solutions can be derived from [OH] using the 1 GPa data derived from pure-H_2O experiments. We use standard states of unit activity of pure minerals at any *P* and *T* and unit fugacity of pure gases at 1 bar and any *T*. With this standard state convention, the low concentrations of TiOOH indicate that $a_{TiO_2} \approx 1$. If the dependence of a_{TiOOH} on TiOOH mole fraction (X_{TiOOH}) can be expressed as

$$a_{TiOOH} = X_{TiOOH}^{n} \tag{4}$$

then Equation 2 can be rewritten:

$$\log K - n \log X_{TiOOH} = \frac{1}{4}\log f_{O_2} - \frac{1}{2}\log f_{H_2O} \tag{5}$$

That is, if Equation 4 is appropriate, then at a given *P* and *T* there should be a linear relationship between $\log X_{TiOOH}$ and the right hand side of Equation 5, with a slope of $-n$ and intercept of $\log K$. Using H_2O fugacity calculated from Holland and Powell (1991), linear least-squares fitting gave high R^2 (≥0.94) at 500, 600, and 800 °C where ≥3 experiments were performed at different f_{O_2}, supporting use of Equation 4. Neglecting the 650 °C data pair, which yielded a highly discrepant slope and intercept, we obtained values of *n* for 1 GPa data of ~2 over the range of experimental *T*. However, substantially improved fitting of the full data set was obtained by letting a_{TiOOH} vary according to

$$n = n_1 + \frac{n_2}{T}. \tag{6}$$

Linear least-squares fitting gave $n_1 = 1.299$, $n_2 = 604.8$ (*T* in Kelvin). Equation 6 yields variation in *n* from 2.1 at 500 °C to 1.8 at 900 °C. The conclusion that $n \approx 2$ implies that a_{TiOOH} is very nearly the square of TiOOH mole fraction. This is sensible in light of our interpretation that Ti reduction is coupled to H substitution, which suggests that the TiO_2-TiOOH solid solution involves mixing on both cation and anion sites. If H is disordered with respect to the six Ti^{3+}-coordinating oxygen sites, then

$$a_{TiOOH} = X_{Ti^{3+}} X_{OH^-} \tag{7}$$

or, by mass balance

$$a_{TiOOH} = X_{TiOOH}^2. \tag{8}$$

The results are thus consistent with nearly ideal, multi-site mixing of the TiO_2-TiOOH solid solution over the conditions of this investigation.

Thermodynamics of OH substitution in rutile

The TiO_2-TiOOH mixing model (Eqs. 7 and 8) allows derivation of the thermodynamic properties of reaction 1 from the data set. Assuming that the activity model is independent of P, we calculated a_{TiOOH} for measured [OH] from pure-H_2O experiments at 800 °C and 0.5, 1.0, and 2.0 GPa, to give log$K$ (Eq. 5) as a function of pressure. The standard volume change of reaction 1, ΔV_r°, was derived from a linear fit to the data and the relation

$$\Delta V_r^\circ = -2.303RT\left(\frac{\partial \log K}{\partial P}\right)_T \quad (9)$$

which gave = 1.90 ± 0.48 cm^3/mol (1σ uncertainty; $R^2 = 0.997$).

Because ΔV_r° is simply the standard volume difference between TiO_2 and TiOOH (see below), it can be assumed independent of P and T and combined with the activity model to compute log$K$ at 1 bar for the pure-H_2O data set. The variation of calculated $\log K_{1\ bar}$ with inverse temperature is described by

$$\log K_{1\ bar} = 1.040 - \frac{11452}{T} \quad (10)$$

where T is again in Kelvin. Thus, from

$$\ln K_{1\ bar} = \frac{\Delta S_r^\circ}{R} - \frac{\Delta H_r^\circ}{RT} \quad (11)$$

we derive ΔS_r°= 19.9 ± 1.4 J/(mol·K) and ΔH_r°= 219.3 ± 1.3 kJ/mol, where ΔS_r° and ΔH_r° are the standard entropy and enthalpy change of reaction 1 at 1 bar.

Table 2 summarizes the parameters derived to describe TiO_2-TiOOH mixing and the thermodynamic properties of reaction 1. These parameters can be used with Equation 9 and

$$\log K = \frac{1}{2.3R}\left(\Delta S_r^\circ - \frac{\Delta H_r^\circ}{T} - \frac{\Delta V_r^\circ}{T}(P-1)\right) = \quad (12)$$

$$n\log X_{TiOOH} + \frac{1}{4}\log f_{O_2} - \frac{1}{2}\log f_{H_2O}$$

to evaluate the quality of the fit, and to compare the energetics of hydrogen substitution in rutile to that in other minerals. Solution of Equation 12 for X_{TiOOH} yields an average absolute deviation from measured X_{TiOOH} of 12.0%. No systematic variation in the deviation was observed with T, P, or f_{O_2} (Fig. 6).

The adopted standard state means that ΔV_r° of 1.90 cm^3/mol corresponds to the volume difference between solids; that is, it is the volume of hydration of TiO_2 to TiOOH. Evidently, substitution of one mole of H accompanying reduction of Ti^{4+} to Ti^{3+} increases the standard volume by 1.90 cm^3/mol, or about 10%. This is nearly identical to the difference in ionic radius of octahedrally coordinated Ti^{4+} and Ti^{3+} of 0.605 and 0.670 Å, respectively (10.7%, Shannon 1976). A ΔV_r° of 1.90 cm^3/mol is lower than that of other nominally anhydrous minerals, which hydrate by a similar substitution mechanism (4.0–11.3 cm^3/mol; Keppler and Bolfan-Casanova 2006). Notably, the lowest ΔV_r° of 4.0 cm^3/mol is associated with Fe^{2+} oxidation to Fe^{3+} in magnesiowüstite (Bolfan-Casanova et al. 2002).

Our ΔH_r° is greater than values previously reported, which are limited to silicate hydration (Keppler and Bolfan-Casanova 2006). The highly endothermic character of reaction 1 is required by the strong temperature dependence exhibited by the data set. Previous studies do not report constraints on reaction entropy. Although the stoichiometry of reaction 1 and the use of gas standard states for H_2O and O_2 lead to the expectation that ΔS_r° should be negative, it is important to note that this parameter is derived by large extrapolation in $1/T$ assuming linear variation of log$K$. While this is reasonable over the experimentally investigated range, it may not be correct over all T. Our derived value of about 20 J/(mol·K) yields steep Clapeyron slopes of log$K$ isopleths. This can be seen in Figure 7a, which gives isopleths of log$K$ for reaction 1 as a function of P and T.

Table 2. Thermodynamic parameters for TiOOH activity and reaction 1

Parameter	Value	1σ
n_1	1.229	
n_2	604.8	
ΔS_r° (J/mol·K)	19.9	1.4
ΔH_r° (kJ/mol)	219.3	1.3
ΔV_r° (cm^3/mol)	1.90	0.48

H-in-rutile thermobarometry and oxybarometry

Equation 12 shows that, in systems with moderate to high X_{H_2O}, the [OH] of nominally pure rutile can be used to extract quantitative information on T, P, and/or f_{O_2}. For example, provided that the trace element content of rutile is low or a correction can be made, Equation 12 can be solved at buffered f_{O_2} to obtain P-T isopleths of rutile [OH] (Figs. 7b–7d). The figures show that measured [OH] due to reaction 1 can be used to infer P or T if the other is known. For example, the observation that the largest [OH] are associated with high-P environments (Johnson 2006) is explained in part by the pattern of isopleths in Figure 7.

Similarly, [OH] in nominally pure rutile can be used as an oxybarometer if P and T are also constrained. For example, Figure 8 shows that, at 1 GPa and temperatures expected for Barrovian or granulite-facies metamorphism, [OH] in rutile is expected to vary from ~50 to several thousand parts per million. Thus, if the trace-element content is low, [OH] in rutile

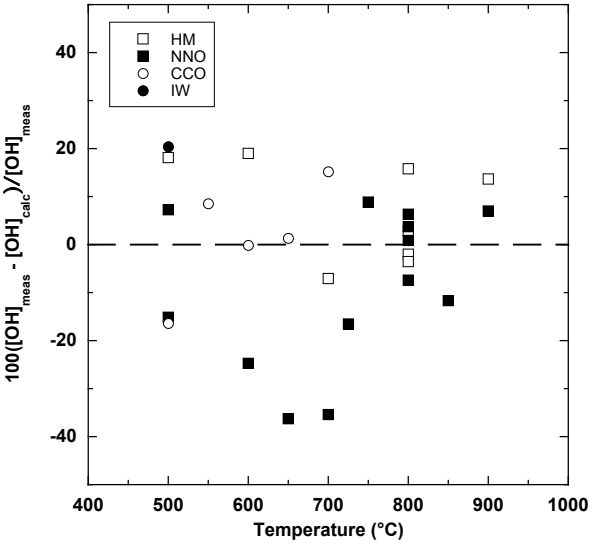

Figure 6. Difference between measured [OH] in experiments of this study and [OH] calculated from Equation 12 and Table 2. Average deviation is 12%. Symbols as in Figure 3.

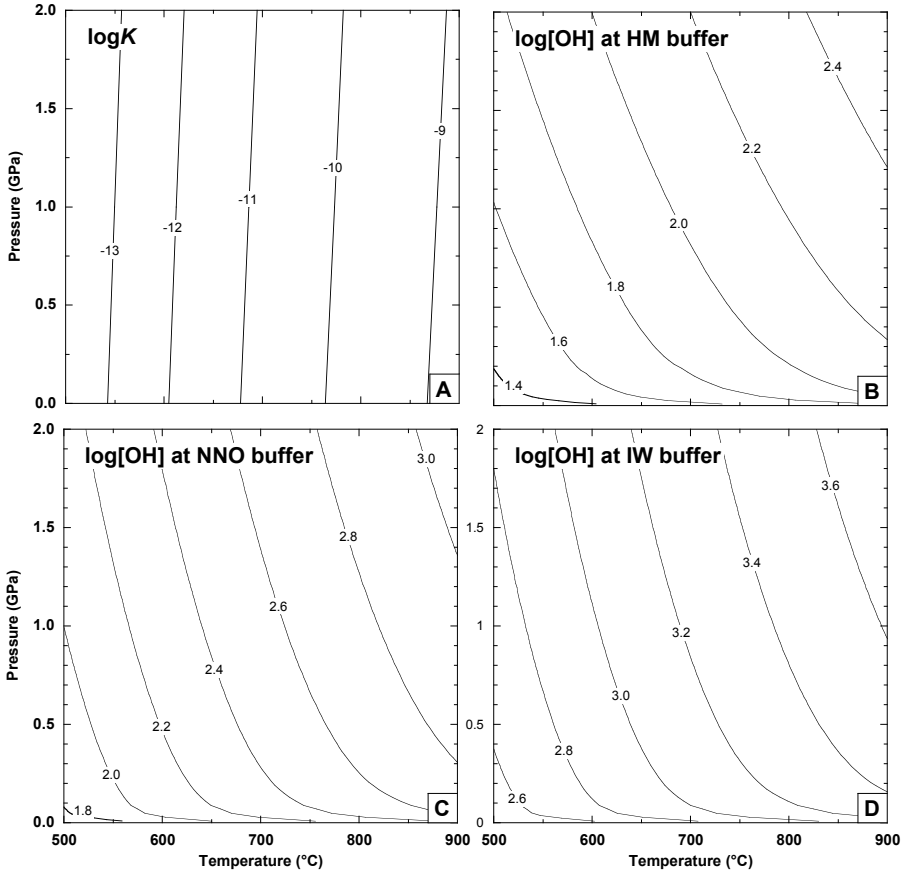

FIGURE 7. Pressure and temperature dependence of the log$K$ for reaction 1 (**a**), and f_{O_2}-buffered [OH] (**b**–**d**), calculated using Equation 12 and data in Table 2. In **d**, the iron-wüstite (IW) buffer is slightly metastable with respect to iron-magnetite equilibrium below ~600 °C.

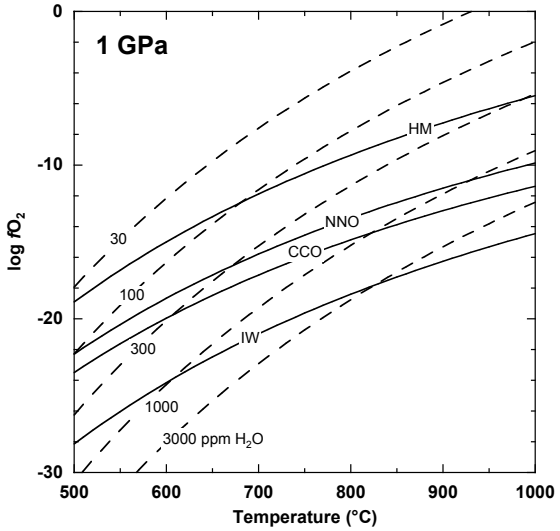

FIGURE 8. Temperature vs. logf_{O_2} at 1 GPa. Solid lines denote the f_{O_2} buffers hematite-magnetite (HM), nickel-nickel oxide (NNO), cobalt-cobalt oxide (CCO), and iron-wüstite (IW). Dashed lines are isopleths of [OH] in rutile calculated from Equation 12 and Table 2. The IW buffer is metastable with respect to iron-magnetite equilibrium below ~600 °C.

can provide a reasonably sensitive monitor of f_{O_2} in mineral assemblages or a wide range of fluid compositions otherwise lacking constraints on this parameter.

Figure 8 suggests that rutile could be deployed in experimental studies as an f_{O_2} sensor, where controlling this parameter is not possible or other sensor techniques (e.g., Chou 1978; Taylor et al. 1992) are impractical. In addition to the sensitivity to f_{O_2} indicated in Figure 8, rutile could be convenient for this purpose because (1) large, synthetic crystals are easily obtained; (2) its tetragonal symmetry facilitiates IR spectroscopic analysis; (3) H solubility is low enough that [OH] can be measured on doubly-polished thin sections of reasonable thicknesses for a wide range of f_{O_2} values (Fig. 4); and (4) the solubility of rutile in water or melts is typically low (e.g., Tropper and Manning 2005; Audétat and Keppler 2005; Antignano and Manning 2008; Manning et al. 2008), so its presence will have minimal effect on the experimental system of interest.

A factor that must be considered in using [OH] in rutile as a thermometer or oxybarometer is the substitution of other elements. Our results show that pure rutile accommodates up to ~1000 ppm H_2O at the f_{O_2} of the CCO and NNO buffers and a broad range of P and T. However, some natural rutile samples contain significantly higher [OH] (Johnson 2006), consistent with additional [OH] related to trivalent cation substitution, adjusted

for the charge-balance effect of pentavalent cation substitution in the structure (Nb^{5+} and Ta^{5+}) (e.g., Vlassopoulos et al. 1993). Further work should be done on synthetic samples to quantify the crystal-chemical effect on OH solubility.

Ti^{3+} in meteorites and terrestrial rutile

The presence of Ti^{3+} in minerals is widely interpreted to be a hallmark of very reducing petrogenetic conditions. Trivalent titanium is an essential structural component of tistarite (Ti_2O_3) and grossmanite ($CaTiAlSiO_6$) from Ca-,Al-rich inclusions (CAIs) of the Allende meteorite (Ma and Rossman 2009a, 2009b). The Ti^{3+} content of CAI grains has been used as an oxybarometer for the low-f_{O_2} environment of the primitive solar nebula (e.g., Beckett and Grossman 1986; Simon et al. 2005). In addition, Ti^{3+} in lunar armalcolite (Smyth 1974; Wechsler et al. 1976) also suggests crystallization at f_{O_2} lower than the iron-wüstite buffer (e.g., Stanin and Taylor 1980). Terrestrial examples of minerals containing significant Ti^{3+} are rare. Ti^{3+}-bearing armalcolite has been reported from highly reducing settings (Tsymbal et al. 1980; Pederson 1981; Mets et al. 1985) and metasomatized mantle xenoliths (e.g., Haggerty 1975, 1983). In many cases, the concentration of Ti^{3+} is inferred indirectly based on calculated charge balance of electron microprobe analyses. Because the charge balance accumulates all analytical errors, the reported Ti^{3+} contents are highly uncertain.

The range in [OH] in Table 1 corresponds to mole fractions of Ti^{3+} in rutile [expressed as $Ti^{3+}O(OH)$] of up to $\sim 4 \times 10^{-3}$. Even at f_{O_2} corresponding to oxidizing conditions of the HM buffer, the Ti^{3+} content of rutile exceeds 0.1 mol% for $T > 800$ °C. Though small, the presence of Ti^{3+} in rutile at T, P, and f_{O_2} encompassing a wide range of terrestrial igneous and metamorphic conditions indicates that caution should be employed in using Ti^{3+} alone as an indicator of reducing conditions.

Acknowledgments

Funding for this work was provided by NSF grant EAR-0538107. The authors would like to thank Bob Newton for help with piston-cylinder experiments, George Rossman for access to the Mineral Spectroscopy Laboratory at Caltech, and the Department of Mineral Sciences, Smithsonian Institution, for access to the FTIR spectrometer. Discussions with Hans Keppler and Bob Newton improved the thermodynamic analysis. We thank Roland Stalder and an anonymous reviewer for insightful comments during journal review.

References cited

Amore Bonapasta, A. Filippone, F., Mattioli, G., and Alippi, P. (2009) Oxygen vacancies and OH species in rutile and anatase TiO_2 polymorphs. Catalysis Today, 144, 177–182.

Antignano, A. and Manning, C.E. (2008) Rutile solubility in H_2O, H_2O-SiO_2 and H_2O-$NaAlSi_3O_8$ at 0.7–2.0 GPa and 700–1000 °C: Implications for mobility of nominally insoluble elements in geologic fluids. Chemical Geology, 255, 283–293.

Aranovich, L.Y. and Newton, R.C. (1999) Experimental determination of CO_2-H_2O activity-composition relations at 600–1000 °C and 6–14 kbar by reversed decarbonation and dehydration reactions. American Mineralogist, 84, 1319–1332.

Audétat, A. and Keppler, H. (2005) Solubility of rutile in subduction zone fluids, as determined by experiments in the hydrothermal diamond anvil cell. Earth and Planetary Science Letters, 232, 393–402.

Ayers, J.C. and Watson, E.B. (1991) Solubility of apatite, monazite, zircon, and rutile in supercritical aqueous fluids with implications for subduction zone geochemistry. Philosophical Transactions of the Royal Society of London, Series A: Mathematical Physical and Engineering Sciences, 335, 365–375.

——— (1993) Rutile solubility and mobility in supercritical aqueous fluids. Contributions to Mineralogy and Petrology, 114, 321–330.

Beckett, J.R. and Grossman, L. (1986) Oxygen fugacities in the solar nebula during crystallization of fassaite in Allende inclusions. Lunar and Planetary Institute, Seventeenth Lunar and Planetary Science Conference Abstracts, 36–37.

Bohlen, S.R., Wall, V.J., and Boettcher, A.L. (1983) Experimental investigations and geological applications of equilibria in the system FeO-TiO_2-Al_2O_3-SiO_2-H_2O. American Mineralogist, 68, 1049–1058.

Bolfan-Casanova, N., Mackwell, S., Keppler, H., McCammon, C., and Rubie, D.C. (2002) Pressure dependence of H solubility in magnesiowüstite up to 25 GPa: implications for the storage of water in Earth's lower mantle. Geophysical Research Letters, 29, 1449, DOI: 10.1029/2001GL014457.

Brenan, J.M., Shaw, H.F., Phinney, D.L., and Ryerson, F.J. (1994) Rutile-aqueous fluid partitioning of Nb, Ta, Hf, Zr, U and Th: implications for high field strength element depletions in island-arc basalts. Earth and Planetary Science Letters, 128, 327–339.

Bromiley, G.D., Hilairet, N., and McCammon, C. (2004) Solubility of hydrogen and ferric iron in rutile and TiO_2 (II): implications for phase assemblages during ultra-high pressure metamorphism and for the stability of silica polymorphs in the lower mantle. Geophysical Research Letters, 31, L04610, DOI: 10.1029/2004GL019430.

Bromiley, G.D. and Hilairet, N. (2005) Hydrogen and minor element incorporation in synthetic rutile. Mineralogical Magazine, 69, 345–358.

Bromiley, G.D. and Shiryaev, A.A. (2006) Neutron irradiation and post-irradiation annealing of rutile (TiO_{2-x}): effect on hydrogen incorporation and optical absorption. Physics and Chemistry of Minerals, 33, 426–434.

Cathcart, J.V., Perkins, R.A., Bates, J.B., and Manley, L.C. (1979) Tritium diffusion in rutile (TiO_2). Journal of Applied Physics, 50, 4110–4119.

Chen, R.-X., Zheng, Y.-F., Gong, B., Zhao, Z.-F., Gao, T.-S., Chen, B., and Wu, Y.-B. (2007) Origin of retrograde fluid in ultrahigh-pressure metamorphic rocks: constraints from mineral hydrogen isotope and water content changes in eclogite-gneiss transitions in the Sulu orogen. Geochimica et Cosmochimica Acta, 71, 2299–2325.

Chou, I.M. (1978) Calibration of oxygen buffers at elevated P and T using the hydrogen fugacity sensor. American Mineralogist, 63, 690–703.

——— (1986) Permeability of precious metals to hydrogen at 2 kb total pressure and elevated temperatures. American Journal of Science, 286, 638–658.

Corfu, F. and Andrews, A.J. (1986) A U-Pb age for mineralized Nipissing diabase, Gowganda, Ontario. Canadian Journal of Earth Science, 23, 107–109.

Diebold, U. (2003) The surface science of titanium dioxide. Surface Science Reports, 48, 53–229.

Filippone, F., Mattioli, G., Alippi, P., and Amore Bonapasta, A. (2009) Properties of hydrogen and hydrogen-vacancy complexes in the rutile phase of titanium dioxide. Physical Review B, 80, 245203.

Foley, S.F., Barth, M.G., and Jenner, G.A. (2000) Rutile/melt partition coefficients for trace elements and an assessment of the influence of rutile on the trace element characteristics of subduction zone magmas. Geochimica et Cosmochimica Acta, 64, 933–938.

Force, E.R. (1980) The provenance of rutile. Journal of Sedimentary Petrology, 50, 485–488.

Frindt, S., Haapala, I., and Pakkanen, L. (2004) Anorogenic Gross Spitzkoppe granite stock in central western Namibia: Part I. Petrology and geochemistry. American Mineralogist, 89, 841–856.

Frost, B.R. (1991) Introduction to oxygen fugacity and its petrologic importance. In D.H. Lindsley, Ed., Oxide Minerals, 25, p. 1–9. Reviews in Mineralogy, Mineralogical Society of America, Chantilly, Virginia.

Haggerty, S.E. (1975) The chemistry and genesis of opaque minerals in Kimberlites, Physics and Chemistry of the Earth, 9, 295–307.

——— (1983) The mineral chemistry of new titanates from Jagersfontein kimberlite, South Africa: Implications for metasomatism in the upper mantle. Geochimica et Cosmochimica Acta, 47, 1833–1854.

Hammer, V.M.F. (1988) Quantitative IR-spectroscopic determination of structural OH-groups in natural rutiles of various occurences. Zeitschrift für Kristallographie, 185, 631.

Hammer, V.M.F. and Beran, A. (1991) Variations in the OH concentration of rutiles from different geological environments. Mineralogy and Petrology, 45, 1–9.

Holland, T.J.B. and Powell, R. (1991) A Compensated Redlich-Kwong equation for volumes and fugacities of CO_2 and H_2O in the range 1 bar to 50 kbar and 100–1600 °C. Contributions to Mineralogy and Petrology, 109, 265–273.

Huebner, J.S. and Sato, M. (1970) The oxygen fugacity-temperature relationships of manganese oxide and nickel oxide buffers. American Mineralogist, 55, 934–952.

Huntington, H.B. and Sullivan, G.A. (1965) Interstitial diffusion mechanism in rutile. Physical Review Letters, 14, 177–178.

Ingrin, J. and Blanchard, M. (2006) Diffusion of hydrogen in minerals. In H. Keppler and J.R. Smyth, Eds., Water in Nominally Anhydrous Minerals, 62, p. 291–320. Reviews in Mineralogy and Geochemistry, Mineralogical Society of America, Chantilly, Virginia.

Johnson, E.A. (2006) Water in nominally anhydrous crustal minerals: speciation, concentration, and geologic significance. In H. Keppler and J.R. Smyth, Eds., Water in Nominally Anhydrous Minerals, 62, p. 117–154. Reviews in Mineralogy and Geochemistry, Mineralogical Society of America, Chantilly, Virginia.

Johnson, O.W., DeFord, J., and Shaner, J.W. (1973) Experimental technique for

the precise determination of H and D concentration in rutile (TiO_2). Journal of Applied Physics, 44, 3008–3012.
Johnson, O.W., Paek, S.H., and DeFord, J.W. (1975) Diffusion of H and D in TiO_2: suppression of internal fields by isotope exchange. Journal of Applied Physics, 46, 1026–1033.
Kapp, P., Manning, C.E., and Tropper, P. (2009) Phase-equilibrium constraints on titanite and rutile activities in mafic epidote amphibolites and geobarometry using titanite-rutile equilibria. Journal of Metamorphic Geology, 27, 509–521.
Katayama, I., Nakashima, S., and Yurimoto, H. (2006) Water content in natural eclogite and implication for water transport into the deep upper mantle. Lithos, 86, 245–259.
Keppler, H. and Bolfan Casanova, N. (2006) Thermodynamics of water solubility and partitioning. In H. Keppler and J.R. Smyth, Eds., Water in Nominally Anhydrous Minerals, 62, p. 193–230. Reviews in Mineralogy and Geochemistry, Mineralogical Society of America, Chantilly, Virginia.
Khomenko, V.M., Langer, K., Rager, H., and Fett, A. (1998) Electronic absorption by Ti^{3+} ions and electron delocalization in synthetic blue rutile. Physics and Chemistry of Minerals, 25, 338–346.
Klemme, S., Prowatke, S., Hametner, K., and Günther, D. (2005) Partitioning of trace elements between rutile and silicate melts: implications for subduction zones. Geochimica et Cosmochimica Acta, 69, 2361–2371.
Lemke, K.H., Rosenbauer, R.J., Bischoff, J.L., and Bird, D.K. (2008) An hydrothermal experimental study of the cobalt-cobalt oxide redox buffer. Chemical Geology, 252, 136–144.
Lu, T.C., Wu, S.Y., Lin, L.B., and Zheng, W.C. (2001) Defects in the reduced rutile single crystal. Physica B, 304, 147–151.
Ma, C. and Rossman, G.R. (2009a) Tistarite, Ti_2O_3, a new refractory mineral from the Allende meteorite. American Mineralogist, 94, 841–844.
——— (2009b) Grossmanite, $CaTi^{3+}AlSiO_6$, a new pyroxene from the Allende meteorite. American Mineralogist, 94, 1491–1494.
Maldener, J., Rauch, F., Gavranic, M., and Beran, A. (2001) OH absorption coefficients of rutile and cassiterite deduced from nuclear reaction analysis and FTIR spectroscopy. Mineralogy and Petrology, 71, 21–29.
Manning, C.E. and Boettcher, S.L. (1994) Rapid-quench hydrothermal experiments at mantle pressures and temperatures. American Mineralogist, 79, 1153–1158.
Manning, C.E. and Bohlen, S.R. (1991) The reaction titanite+kyanite=anorthite+rutile and titanite-rutile barometry in eclogites. Contributions to Mineralogy and Petrology, 109, 1–9.
Manning, C.E., Wilke, M., Schmidt, C., and Cauzid, J. (2008) Rutile solubility in albite-H_2O and $Na_2Si_3O_7$-H_2O at high temperatures and pressures by in-situ synchrotron radiation micro-XRF. Earth and Planetary Science Letters, 272, 730–737.
McCanta, M.C., Dyar, M.D., Rutherford, M.J., and Delaney, J.S. (2004) Iron partitioning between basaltic melts and clinopyroxene as a function of oxygen fugacity. American Mineralogist, 89, 1685–1693.
Mets, O.F., Polezhayeva, L.I., and Bogdanova, A.N. (1985) Armalcolite from microcline-plagioclase pegmatites of the Kola Peninsula. International Geology Review, 27, 1470–1480.
Mezger, K., Hanson, G.N., and Bohlen, S.R. (1989) High-precision U-Pb ages of metamorphic rutile—application to the cooling history of high-grade terranes. Earth and Planetary Science Letters, 96, 106–118.
Mezger, K., Rawnsley, C.M., Bohlen, S.R., and Hanson, G.N. (1991) U-Pb garnet, sphene, monazite, and rutile ages: implications for the duration of high-grade metamorphism and cooling histories, Adirondack Mts., New York. Journal of Geology, 99, 415–428.
Newton, R.C. and Manning, C.E. (2000) Quartz solubility in H_2O-NaCl and H_2O-CO_2 solutions at deep crust-upper mantle pressures and temperatures: 2-15 kbar and 500-900 °C. Geochimica et Cosmochimica Acta, 64, 2993–3005.
Pederson, A.K. (1981) Armalcolite-bearing Fe-Ti oxide assemblages in graphite-equilibrated salic volcanic rocks with native iron from Disko, central west Greenland. Contributions to Mineralogy and Petrology, 77, 307–324.
Rossman, G.R. and Smyth, J.R. (1990) Hydroxyl contents of accessory minerals in mantle eclogites and related rocks. American Mineralogist, 75, 775–780.
Rudnick, R.L., Barth, M., Horn, I., and McDonough, W.F. (2000) Rutile-bearing refractory eclogites: missing link between continents and depleted mantle. Science, 287, 278–281.
Ryerson, F.J. and Watson, E.B. (1987) Rutile saturation in magmas: implications for Ti-Nb-Ta depletion in island-arc basalts. Earth and Planetary Science Letters, 86, 225–239.
Shannon, R.D. (1976) Revised effective ionic radii and systematic studies of interatomic distances in halides and chalcogenides. Acta Crystallographica, 32, 751–767.
Simon, J.I., Young, E.D., Russell, S.S., Tonui, E.K., Dyl, K.A., and Manning, C.E. (2005) A short timescale for changing oxygen fugacity in the solar nebula revealed by high-resolution ^{26}Al-^{26}Mg dating of CAI rims. `Earth and Planetary Science Letters, 238, 272–283.
Sorensen, S.S. and Grossman, J.N. (1993) Accessory minerals and subduction zone metasomatism: a geochemical comparison of two mélanges (Washington and California, U.S.A.). Chemical Geology, 110, 269–297.
Smyth, J.R. (1974) The crystal chemistry of armalcolites from Apollo 17. Earth and Planetary Science Letters, 24, 262.
Spencer, K.J. and Lindsley, D.H. (1981) A solution model for coexisting iron-titanium oxides. American Mineralogist, 66, 1189–1201.
Stalder, R., Foley, S.F., Brey, G.P., and Horn, I. (1998) Mineral-aqueous fluid partitioning of trace elements at 900-1200 °C and 3.0-5.7 GPa: new experimental data for garnet, clinopyroxene and rutile, and implications for mantle metasomatism. Geochimica et Cosmochimica Acta, 62, 1781–1801.
Stanin F.T. and Taylor L.A. (1980) Armalcolite: an oxygen fugacity indicator. Lunar and Planetary Institute, Eleventh Lunar and Planetary Science Conference Abstracts, 117–124.
Swope, R.J., Smyth, J.R., and Larson, A.C. (1995) H in rutile-type compounds: I. Single-crystal neutron and X-ray diffraction study of H in rutile. American Mineralogist, 80, 448–453.
Taylor, J.R., Wall, V.J., and Pownceby, M.I. (1992) The calibration and application of accurate redox sensors. American Mineralogist, 77, 284–295.
Thompson, T.L. and Yates, J.T. Jr. (2006) Surface science studies of the photoactivation of TiO_2—New photochemical processes. Chemical Reviews, 106, 4428–4453.
Tomkins, H.S., Powell, R., and Ellis, D.J. (2007) The pressure dependence of the zirconium-in-rutile thermometer. Journal of Metamorphic Geology, 25, 703–713.
Triebold, S., von Eynatten, H., Luvizotto, G.L., and Zack, T. (2007) Deducing source rock lithology from detrital rutile geochemistry; an example from the Erzgebirge, Germany. Chemical Geology, 244, 421–436.
Tropper, P. and Manning, C.E. (2005) Very low solubility of rutile in H_2O at high pressure and temperature, and its implications for Ti mobility in subduction zones. American Mineralogist, 90, 502–505.
——— (2008) The current status of titanite-rutile thermobarometry in ultrahigh-pressure metamorphic rocks: the influence of titanite activity models on phase equilibrium calculations. Chemical Geology, 254, 123–132.
Tsymbal, S.N., Tatarintsev, V.I., Legkova, G.V., and Yegorova, L.N. (1980) Armalcolite: The first occurrence in the USSR. Mineralogiya Zhurnal, 2, 87–95 (in Russian).
Vlassopoulos, D., Rossman, G.R., and Haggerty, S.E. (1993) Coupled substitution of H and minor elements in rutile and the implications of high OH contents in Nb- and Cr-rich rutile from the upper mantle. American Mineralogist, 78, 1181–1191.
Watson, E.B. and Harrison, T.M. (2005) Zircon thermometer reveals minimum melting conditions on earliest Earth. Science, 308, 841–844.
Watson, E.B., Wark, D.A., and Thomas, J.B. (2006) Crystallization thermometers for zircon and rutile. Contributions to Mineralogy and Petrology, 151, 413–433.
Wechsler, B.A., Prewitt, C.T., and Papike, J.J. (1976) Chemistry and structure of lunar and synthetic armalcolite. Earth and Planetary Science Letters, 29, 91–103.
Zack, T. and Luvizottow, G.L. (2006) Application of rutile thermometry to eclogites. Mineralogy and Petrology, 88, 69–85.
Zack, T., Kronz, A., Foley, S.F., and Rivers, T. (2002) Trace element abundances in rutiles from eclogites and associated garnet mica schists. Chemical Geology, 184, 97–122.
Zack, T., Moraes, R., and Kronz, A. (2004a) Temperature dependence of Zr in rutile: empirical calibration of a rutile thermometer. Contributions to Mineralogy and Petrology, 148, 471–488.
Zack, T., von Eynatten, H., and Kronz, A. (2004b) Rutile geochemistry and its potential use in quantitative provenance studies. Sedimentary Geology, 171, 37–58.
Zhang, J.F., Jin, Z.M., Green, H.W. II, and Jin, S.Y. (2001) Hydroxyl in continental deep subduction zone: Evidence from UHP eclogites of the Dabie Mountains. Chinese Science Bulletin, 46, 592–595.
Zhang, J.F., Green, H.W. II, Bozhilov, K., and Jin, S.Y. (2004) Faulting induced by precipitation of water at grain boundaries in hot subducting oceanic crust. Nature, 428, 633–636.
Zhao, Z.F., Chen, B., Zheng, Y.F., Chen, R.X., and Wu, Y.B. (2007) Mineral oxygen isotope and hydroxyl content changes in ultrahigh-pressure eclogite-gneiss contacts from Chinese Continental Scientific Drilling Project cores. Journal of Metamorphic Geology, 25, 165–186.
Zheng, Y.F. (2009) Fluid regime in continental subduction zones: petrological insights from ultrahigh-pressure metamorphic rocks. Journal of the Geological Society, London, 166, 763–782.

Manuscript received September 30, 2010
Manuscript accepted April 21, 2011
Manuscript handled by Simon Redfern